

# In Search of the First Stars: An Ultra-Compact and Very Low Metallicity Lyman- $\alpha$ Emitter Deep Within the Epoch of Reionization

CHRIS J. WILLOTT <sup>1</sup>, YOSHIHISA ASADA <sup>2,3</sup>, KARTHEIK G. IYER <sup>4</sup>, JON JUDEŽ <sup>5</sup>, GREGOR RIHTARŠIČ <sup>5</sup>,  
NICHOLAS S. MARTIS <sup>5</sup>, GHASSAN T. E. SARROUH <sup>6</sup>, GUILLAUME DESPREZ <sup>7</sup>, ANISHYA HARSHAN <sup>5</sup>,  
LAMIYA MOWLA <sup>8</sup>, GAËL NOIROT <sup>9</sup>, GIORDANO FELICIONI <sup>5</sup>, MARUŠA BRADAČ <sup>5,10</sup>, GABE BRAMMER <sup>11,12</sup>,  
ADAM MUZZIN <sup>6</sup>, MARCIN SAWICKI <sup>2</sup>, JACQUELINE ANTWI-DANSO <sup>13</sup>, VLADAN MARKOV <sup>5</sup> AND  
ROBERTA TRIPODI <sup>5,14</sup>

<sup>1</sup>*NRC Herzberg, 5071 West Saanich Rd, Victoria, BC V9E 2E7, Canada*

<sup>2</sup>*Department of Astronomy and Physics and Institute for Computational Astrophysics, Saint Mary's University, 923 Robie Street, Halifax, Nova Scotia B3H 3C3, Canada*

<sup>3</sup>*Department of Astronomy, Kyoto University, Sakyo-ku, Kyoto 606-8502, Japan*

<sup>4</sup>*Columbia Astrophysics Laboratory, Columbia University, 550 West 120th Street, New York, NY 10027, USA*

<sup>5</sup>*University of Ljubljana, Department of Mathematics and Physics, Jadranska ulica 19, SI-1000 Ljubljana, Slovenia*

<sup>6</sup>*Department of Physics and Astronomy, York University, 4700 Keele St. Toronto, Ontario, M3J 1P3, Canada*

<sup>7</sup>*Kapteyn Astronomical Institute, University of Groningen, P.O. Box 800, 9700AV Groningen, The Netherlands*

<sup>8</sup>*Whitin Observatory, Department of Physics and Astronomy, Wellesley College, 106 Central Street, Wellesley, MA 02481, USA*

<sup>9</sup>*Space Telescope Science Institute, 3700 San Martin Drive, Baltimore, Maryland 21218, USA*

<sup>10</sup>*Department of Physics and Astronomy, University of California Davis, 1 Shields Avenue, Davis, CA 95616, USA*

<sup>11</sup>*Cosmic Dawn Center (DAWN), Denmark*

<sup>12</sup>*Niels Bohr Institute, University of Copenhagen, Jagtvej 128, DK-2200 Copenhagen N, Denmark*

<sup>13</sup>*David A. Dunlap Department of Astronomy and Astrophysics, University of Toronto, 50 St. George Street, Toronto, Ontario, M5S 3H4, Canada\**

<sup>14</sup>*INAF - Osservatorio Astronomico di Roma, Via Frascati 33, Monte Porzio Catone, 00078, Italy*

## ABSTRACT

We present *JWST* observations of a gravitationally-lensed, extremely metal-poor galaxy at redshift  $z = 8.203 \pm 0.001$  from the CANUCS survey. Based on the low oxygen to Balmer line ratios we infer a gas-phase metallicity of  $12 + \log(\text{O}/\text{H}) = 6.85$  (1.4% solar), making CANUCS-A370-z8-LAE the most metal-poor galaxy known at  $z > 7$ . With a high  $\text{H}\beta$  equivalent width of  $225 \pm 50 \text{ \AA}$  and a half-light radius of only  $r_{\text{hl}} = 38_{-19}^{+3} \text{ pc}$ , the galaxy has a high star-formation-rate density of  $50 - 100 M_{\odot} \text{ yr}^{-1} \text{ kpc}^{-2}$ . The galaxy shows high equivalent width Lyman- $\alpha$  emission with an inferred Lyman- $\alpha$  escape fraction of  $0.21 \pm 0.05$ . The high escape fraction of Lyman- $\alpha$  is likely due to the compact starbursting nature of the galaxy combined with its location in an overdensity traced by at least two other galaxies spectroscopically confirmed to lie within  $\delta z = 0.01$  that have helped to reionize the environment. The low metallicity of CANUCS-A370-z8-LAE is best explained by a model where infalling metal-poor gas dilutes the interstellar medium, rather than being a young galaxy forming its first stellar populations.

*Keywords:* galaxies: high-redshift — galaxies: evolution — galaxies: formation

## 1. INTRODUCTION

A key goal for the *James Webb Space Telescope* (*JWST*, Gardner et al. 2023) is to identify the first pop-

ulations of stars that arose from pristine gas, devoid of heavy elements, the so-called Population III. The first stars are expected to be extremely massive with very short lifetimes that end in violent supernovae (Bromm et al. 1999). Consequently, galaxies rapidly become enriched in heavy elements, and finding galaxies with a high star formation rate (SFR) and no metals will be

chris.willott@nrc.ca

\* Banting Postdoctoral Fellow

difficult (Katz et al. 2023). The best prospects for detecting Population III objects may therefore be from the first supernovae strongly magnified by gravitational lensing (Windhorst et al. 2018; Venditti et al. 2024) or in very low mass regions discovered adjacent to more enriched galaxies (Rydberg et al. 2013; Zackrisson et al. 2015).

Spectroscopic observations with *JWST* have allowed the measurement of metallicities for hundreds of high-redshift galaxies. However, rather surprisingly, only shallow evolution towards lower metallicities at high redshifts has been observed (Nakajima et al. 2023; Curti et al. 2024; Sanders et al. 2024; Langeroodi & Hjorth 2024). The typical metallicity of galaxies at redshifts 7 to 9 (corresponding to 750 to 500 million years after the Big Bang) is 10% times the solar abundance, with almost all galaxies in this redshift range having metallicity in the range 3% to 30% solar, and a well-developed mass-metallicity relation already in place (Nakajima et al. 2023; Curti et al. 2024). This may be indicative of a *metallicity floor* due to the aforementioned rapid enrichment provided by the first very massive stars (Wise et al. 2012; Nishigaki et al. 2023).

The lowest metallicity reionization-era object measured so far is the  $z = 6.6$  Lyman- $\alpha$  emitter LAP-1 (Vanzella et al. 2023). This strongly-lensed object is likely a single star cluster with very low mass of only about  $10,000 M_{\odot}$  and metallicity estimated to be less than 0.4% solar. Fujimoto et al. (2025) additionally report a lensed  $z = 6.5$  low-mass galaxy that may have metallicity less than 1% solar based on model fitting to the photometry. This may indicate that to find the first stars one has to look at strongly-lensed galaxies that have low stellar masses and where individual star-forming regions with different metallicities may be separated.

In the local universe, low-metallicity, low-mass galaxies are often very strong emitters of Lyman- $\alpha$  photons (Izotov et al. 2024) and Lyman continuum ionizing radiation (Annibali & Tosi 2022). High-redshift analogs of these galaxies may therefore be important contributors to the process of cosmic reionization. Strong Lyman- $\alpha$  emission is, however, rarely observed at redshifts  $z > 7$  due to absorption by intervening neutral hydrogen in the intergalactic medium (Stark et al. 2010; Tang et al. 2024; Jones et al. 2025). When high Lyman- $\alpha$  escape fractions are observed, calculation of the ionized bubble size to allow transmission usually requires UV ionizing continuum from multiple galaxies in an overdensity (Saxena et al. 2023; Jung et al. 2024; Chen et al. 2024; Witstok et al. 2025). Therefore, Lyman- $\alpha$  transmission at this epoch often requires favorable conditions on both the

galaxy-scale and proto-cluster scale (e.g. Witten et al. 2024).

In this paper we discuss the galaxy CANUCS-A370-z8-LAE that we have identified from NIRC*am* imaging and follow-up NIRS*pec* spectroscopy to be a very compact and strongly-lensed galaxy displaying both Lyman- $\alpha$  emission and very low metallicity nebular gas at a redshift of  $z = 8.203 \pm 0.001$ . This galaxy was first identified from Hubble Frontier Fields imaging (Lotz et al. 2017) in Abell 370. In Ishigaki et al. (2018) it is object HFF6C-5187-5411 with  $z_{\text{phot}} = 7.38^{+0.82}_{-5.89}$  and lensing magnification of 17.57. Yang et al. (2022) adopted  $z_{\text{phot}} = 7.70$  and fit a source-plane effective radius of  $r_e = 0.07 \pm 0.03$  kpc; one of the smallest  $z \approx 8$  galaxies in their sample.

In Section 2 we present the data used in this work. Section 3 describes the physical inferences made possible by these data. Section 4 discusses the nature of this galaxy and its implications. In Section 5 we give our conclusions. We assume a flat  $\Lambda$ CMD cosmology, with  $\Omega_{\Lambda} = 0.7$ ,  $\Omega_{\text{m}} = 0.3$ , and  $H_0 = 70 \text{ km s}^{-1} \text{ Mpc}^{-1}$ . Magnitudes are given in the AB system (Oke & Gunn 1983).

## 2. DATA

### 2.1. Imaging

We observed CANUCS-A370-z8-LAE in imaging mode with the NIRC*am* (Rieke et al. 2023) and NIRS*ISS* (Doyon et al. 2023) instruments as part of the JWST Cycle 1 program CANUCS (Willott et al. 2022) in December 2022. NIRC*am* observations were made in the F090W, F115W, F150W, F200W, F277W, F356W, F410M and F444W filters for 6.4 ks each. With NIRS*ISS* the F115W, F150W and F200W filters were used for 2.3 ks each. The data were processed along with the existing *HST* imaging as described in earlier CANUCS papers (Desprez et al. 2024; Willott et al. 2024, see also Sarrouh and Asada et al. in prep.). Mosaic images are generated by drizzling onto pixel scales of 40 milli-arcsec for source detection and photometry. The NIRC*am* Short-Wave (SW) images are also drizzled onto a 20 milli-arcsec scale for morphological analysis. From the resulting photometric catalog, this galaxy has an EA*z*Y-Py (Brammer et al. 2008) photometric redshift of  $z_{\text{phot}} = 7.93^{+0.17}_{-0.06}$ . This photometric redshift fitting followed the method of Asada et al. (2024) using templates with strong emission lines and increased neutral hydrogen absorption at  $z > 7$ .

### 2.2. Spectroscopy

The Abell 370 field was observed on 5 September 2023 with NIRS*pec* low-resolution prism follow-up us-

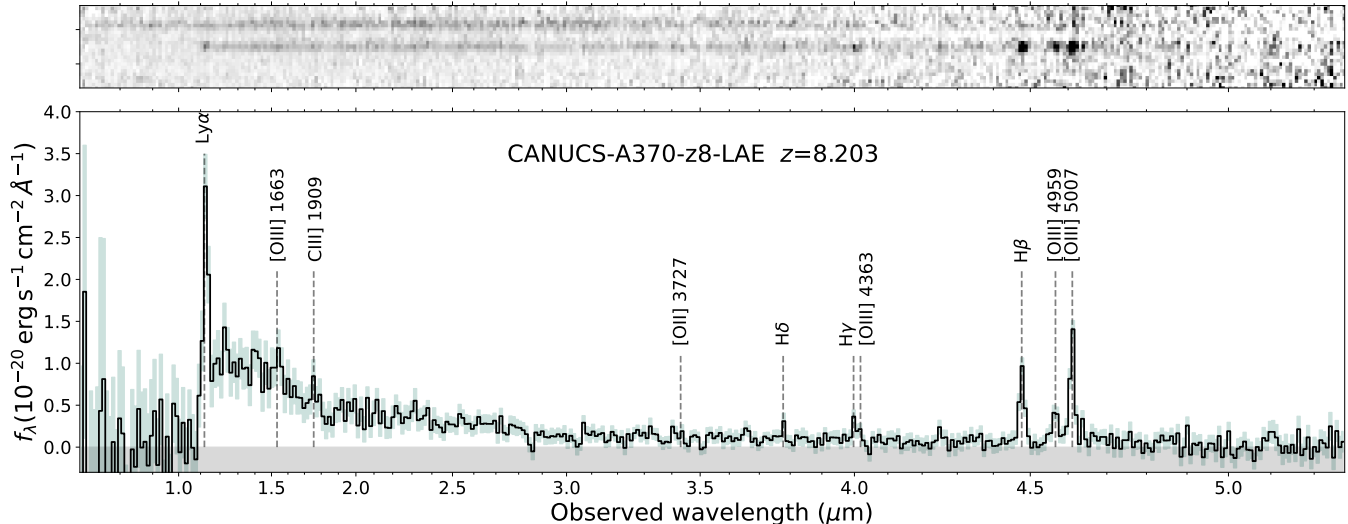


**Figure 1.** NIRSpec prism spectrum of CANUCS-A370-z8-LAE. The upper panel shows the 2D spectrum of the target in the central row with a lower redshift galaxy spectrum near the top of the panel. Several emission lines, including Lyman- $\alpha$ , are clearly visible in the 2D spectrum. The lower panel shows a 1D optimal extraction. Expected strong emission lines are labeled. As well as strong Lyman- $\alpha$ , this spectrum is notable for the very high ratios of H $\beta$  to [O III]  $\lambda$ 5007 and [O III]  $\lambda$ 5007 to [O II]  $\lambda$ 3727, indicative of a very low gas-phase metallicity.

ing the Micro-Shutter Assembly (MSA, Ferruit et al. 2022) as part of the CANUCS program. Strongly-lensed  $z > 7$  galaxies were targeted with high priority to study the stellar populations and ISM conditions in low-mass galaxies within the Epoch of Reionization. Three MSA configurations were observed to enable the large gaps between the four MSA quadrants to be dithered across. Each configuration was observed for 2.9 ks with the targets nodded along a 3-shutter slitlet. CANUCS-A370-z8-LAE was included in all 3 MSA configurations, so the total exposure time was 8.7 ks.

Details of the NIRSpec processing are given in Desprez et al. (2024). For this galaxy we use a version of the `msaexp` package (Brammer 2022) with master background subtraction to avoid over-subtraction due to a nearby galaxy along the slitlet in some nod positions. The wavelength solution accounts for the intra-shutter location of the target. A one-dimensional (1D) optimal extraction is performed from the combined two-dimensional (2D) spectrum. A slitloss correction is applied based on a polynomial fit to the NIRCcam photometry. Flux uncertainties in NIRSpec prism spectra from the pipeline are known to be underestimated due to inter-pixel correlations and non-Gaussian noise (Arrabal Haro et al. 2023). We test for this by extracting line fluxes and errors at random positions in the 1D spectrum. We find a factor of 1.5 increase in uncertainty is required to bring the number of false identifications at  $> 2\sigma$  in line with expectations, so we multiply the error array by this value.

The 2D and 1D spectra of CANUCS-A370-z8-LAE are shown in Figure 1. Strong emission lines typical of galaxies at these redshifts such as [O III], H $\beta$  and H $\gamma$  are visible. The ratio of H $\beta$  to [O III]  $\lambda$ 5007 is unusually high. The [O II]  $\lambda$ 3727 line is not detected, so the high [O III]  $\lambda$ 5007 to [O II]  $\lambda$ 3727 ratio indicates a high ionization parameter. Together, these results indicate a very low oxygen abundance in the nebular gas (e.g. Nakajima et al. 2022), as will be discussed in Section 4.1.

Another unusual aspect of this spectrum is the appearance of strong Lyman- $\alpha$  emission. Strong Lyman- $\alpha$  emission is only visible in the NIRSpec low-resolution prism spectra for 10% of  $z \approx 8$  galaxies (Jones et al. 2025). Given the highly neutral state of the intergalactic medium (IGM) at this epoch (Planck Collaboration et al. 2020) this suggests that CANUCS-A370-z8-LAE resides within a large ionized bubble that allows Lyman- $\alpha$  radiation to escape.

### 3. MEASUREMENTS

#### 3.1. Spectral Fitting

We fit spectral regions near emission lines using the Levenberg-Marquardt non-linear least-squares algorithm. This method returns uncertainties that account for the covariance between parameters. Results of fitting the 1D spectrum are shown in Figure 2. The Lyman- $\alpha$  spectral regions of galaxies at this epoch are complex owing to Lyman- $\alpha$  absorption from nearby regions that can have a range of density and neutral fraction com-

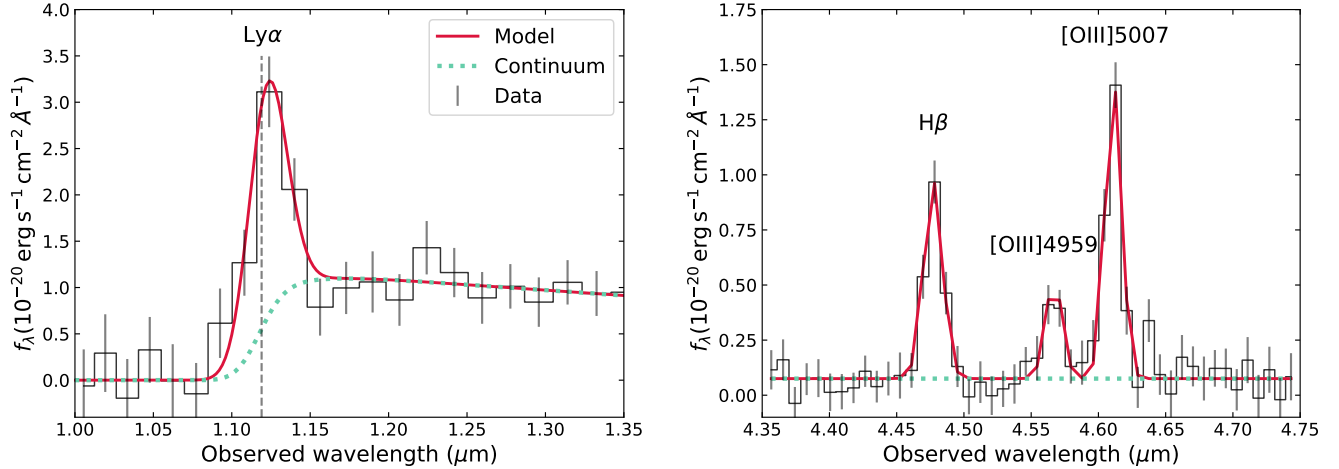


**Figure 2.** Emission line fits (red lines) for CANUCS-A370-z8-LAE compared to the data (black steps with  $1\sigma$  uncertainties). Left: The Lyman- $\alpha$  line is modeled as a Gaussian at the systemic redshift (marked by the dashed vertical line) added to an underlying  $\beta = -1.8$  UV continuum. This model is subjected to absorption from a fully neutral IGM with the galaxy at the center of a 2 pMpc radius ionized bubble. The full model is convolved with the NIRSpc prism line spread function and then rebinned to the observed spectral resolution before fitting. The continuum contribution is shown as a green dotted line. Right: Gaussian fits to the observed H $\beta$  and [O III] lines show very strong H $\beta$  emission that is not broader than the [O III] emission, arguing against an AGN broad line explanation for the strong H $\beta$  emission.

bined with Lyman- $\alpha$  emission that is resonantly scattered. Given the moderate S/N of our spectrum we are unable to simultaneously constrain the properties of the IGM, an adjacent damped Lyman- $\alpha$  absorber and an ionized bubble. From the presence of strong Lyman- $\alpha$  emission we expect minimal effect from any proximate damped Lyman- $\alpha$  absorber (although examples of such cases do exist and require the Lyman- $\alpha$  emission to be offset from the continuum, e.g. Witstok et al. 2024). However, in the case of CANUCS-A370-z8-LAE there is not a strong downturn in the UV continuum near Lyman- $\alpha$  that would be expected for a high column density absorber.

We set the intrinsic Lyman- $\alpha$  emission to be a Gaussian at the systemic redshift determined via fitting the rest-optical lines. Any velocity offset within the galaxy would be much less than one pixel at this wavelength ( $4000 \text{ km s}^{-1}$ ) so can be neglected. We model the continuum as a power-law with  $\beta = -1.8 \pm 0.15$  (where  $f_\lambda \propto \lambda^\beta$ ) based on a fit to the NIRCcam photometry at rest-frame 1500 to 3400  $\text{\AA}$ . As mentioned previously, the spectral S/N is not high enough to constrain the IGM neutral fraction,  $x_{\text{HI}}$ , and fully-ionized bubble size,  $R_{\text{ion}}$ , but setting  $x_{\text{HI}} = 1$  and  $R_{\text{ion}} = 2 \text{ pMpc}$  allows a good fit of a combined line plus continuum model to the data. This model is generated at higher spectral resolution, convolved with the NIRSpc prism line spread function (including a correction factor of 1.6 due to this compact source under-filling the shutter as in de Graaff et al. 2024) and rebinned to the pixel sampling of the data.

The parameters of the continuum amplitude, Lyman- $\alpha$  flux and Lyman- $\alpha$  Gaussian dispersion are left as free parameters. From the fit we calculate the Lyman- $\alpha$  rest-frame equivalent width to be  $\text{EW}(\text{Ly}\alpha) = 63 \pm 9 \text{ \AA}$ . The reduced  $\chi^2$  is 0.62, indicating a good fit and that the flux uncertainties may be a little too high in this region of the spectrum.

The rest-frame optical lines of H $\beta$  and [O III] are plotted in the right panel of Figure 2. All three lines are simultaneously fit by observed Gaussians at a single redshift. In this case we do not fit a higher resolution model convolved with the line spread function. The ratios of [O III]  $\lambda 4959$  and [O III]  $\lambda 5007$  are constrained by their known ratio of 2.98 from atomic physics. The free parameters are the redshift, a constant continuum level, Gaussian line amplitudes and observed dispersions of [O III] and H $\beta$ . The redshift resulting from this fit is  $z = 8.203 \pm 0.001$ . We find an observed Gaussian dispersion of  $69 \pm 8 \text{ \AA}$  for H $\beta$  and  $61 \pm 6 \text{ \AA}$  for [O III]. Based on the prism dispersion change with wavelength we would expect the H $\beta$  dispersion to be 7% greater than that of [O III]  $\lambda 5007$ . We find it to be 11% greater, but the difference is well within the  $1\sigma$  uncertainties. Since the FWHM of these lines are consistent, we find no evidence for an AGN broad-line region in CANUCS-A370-z8-LAE. The H $\beta$  rest-frame equivalent width is  $\text{EW}(\text{H}\beta) = 225 \pm 50 \text{ \AA}$  placing this galaxy in the high  $\text{EW}(\text{H}\beta)$  class of galaxies according to Nakajima et al. (2022).

We fit other important emission lines in a similar manner.  $H\gamma$  and  $[\text{O III}]\lambda 4363$  are partially blended at the spectral resolution of the prism. However, the fluxes of both lines can often be well constrained at  $z > 8$  with high enough S/N data, due to the increase in spectral resolution toward the red end of the prism wavelength range (e.g. Hsiao et al. 2024; Mowla et al. 2024; Tripodi et al. 2024). Given the low oxygen abundance and faintness of this galaxy,  $[\text{O III}]\lambda 4363$  is not significantly detected and we are unable to place a strong limit on the ratio of  $[\text{O III}]\lambda 4363$  to  $[\text{O III}]\lambda 5007$  and hence the electron temperature. There is a peak in the 1D spectrum at the expected position of  $\text{O III}]\lambda 1667$ , but given the low significance and possible blending with  $\text{He II}$  we do not fit that line. Also in the UV, there is a single pixel spike at the expected wavelength of  $\text{C III}]\lambda 1909$ , but further data would be required to confirm a significant detection.

The unblended  $H\delta$  line is fit in order to determine a Balmer decrement in combination with  $H\beta$ . We find a ratio of  $H\delta$  to  $H\beta$  of  $0.19 \pm 0.08$ . This is within  $1\sigma$  of the value of 0.25 that is expected for case B with no dust reddening. Considering also the presence of strong Lyman- $\alpha$  emission in the observed spectrum, we assume no dust reddening of the nebular gas.

The low ionization  $[\text{O II}]\lambda 3727$  line is not significantly detected. We determine a  $2\sigma$  upper limit from fitting the spectrum at the expected position and use this to derive a lower limit on the ratio of  $[\text{O III}]\lambda 5007$  to  $[\text{O II}]\lambda 3727$  of  $\text{O32} > 8.8$ , indicating very high ionization, consistent with the known correlation between  $\text{O32}$  and  $\text{EW}(H\beta)$  (Nakajima et al. 2022). The results of emission line fitting are given in Table 1.

### 3.2. Lensing Modeling

We use the CANUCS gravitational lensing model of the Abell 370 cluster (Gledhill et al. 2024) to derive the magnification and enable a source-plane morphology analysis. The lensing model is not highly constrained in this region due to a lack of multiple images nearby and a massive elongated mass component accounting for the southern overdensity of cluster galaxies. The best-fit lensing magnification at the location and redshift of CANUCS-A370-z8-LAE is  $\mu = 8.0$ . The uncertainty in the lensing model is derived from 100 randomly drawn lens models from the Bayesian sample of the Monte-Carlo Markov-Chain run (see Gledhill et al. 2024 for details). The distribution of acceptable models in these 100 random draws has a wide range from  $9.6 < \mu < 21.8$  at 68% confidence. We note that the best-fit model is not contained within the  $1\sigma$  range, as the likelihood distribution is not symmetric, with the lowest  $\chi^2$  values

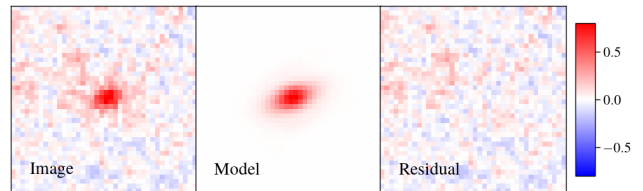


**Figure 3.** Left: NIRCcam F200W image of CANUCS-A370-z8-LAE on a 20 milli-arcsec pixel scale in units of nJy per pixel. The field shown is 0.8 arcsec. The galaxy appears slightly elongated at a position angle close to the lensing shear direction of  $108^\circ$ . Middle: Lenstruction model reconstruction of a zero ellipticity Sérsic  $n = 1$  model with half-light radius = 8 milliarcsec. This reconstruction is for the best fit lensing model ( $\mu = 8.0$ ). Right: Residual image showing that this model fully represents the flux distribution of CANUCS-A370-z8-LAE. The small excess of positive flux in the north-east quarter of the image may be due to extended emission from CANUCS-A370-z8-LAE or, more likely, a foreground galaxy to the north-east that lies just outside the cutout.

tending to lie at the low end of the magnification range, rather than near the median. To be conservative, we adopt the best-fit magnification  $\mu = 8.0$  as our default. However, for the morphology analysis in the next section we will additionally use all 100 iterations of the model to include the lensing uncertainty.

### 3.3. Morphology Fitting

CANUCS-A370-z8-LAE is extremely compact in NIRCcam imaging, despite being strongly lensed with  $\mu \approx 8$ . The lensing field at this location is highly tangential, with the tangential component of the magnification equal to  $\approx 7$ . CANUCS-A370-z8-LAE appears marginally resolved along this direction in the NIRCcam SW images in the F150W and F200W filters. It does not appear resolved in the radial direction, consistent with a small intrinsic size.

We derive a size estimate for the galaxy by fitting the F200W image which has the highest S/N of the SW filters. We use the F200W mosaic image that has been drizzled onto a pixel scale of 20 milli-arcsec (c.f. the native pixel scale is 33 milli-arcsec). We use Lenstruction (Birrer et al. 2015; Birrer & Amara 2018; Yang et al. 2020) which is a source reconstruction tool based on forward modeling the appearance of the source in the image plane accounting for the distortion by lensing and the instrumental point spread function (PSF). The surface brightness distribution in the source plane is approximated by a two-dimensional elliptical Sérsic profile. Lenstruction employs a Bayesian inference formalism to estimate the full posterior distribution of all source model parameters. We use a 20 milli-arcsec empirical

PSF generated using the procedure described in Sarrouh and Asada et al. (in prep.).

Fitting lensed galaxies with a highly tangential deflection field leads to strong size constraints along one axis only. The resulting best-fit shapes are often elongated perpendicular to the shear, due to this lack of constraint and that is what we find when we leave the shape unconstrained. We therefore assume that the source-plane shape has zero ellipticity to estimate the most likely size along both axes. Under this assumption, and fixing the Sérsic index to  $n = 1$ , we measure an intrinsic (before lensing) half-light radius of  $r_{\text{hl}} = 8.0_{-4.0}^{+0.7}$  milliarcsec. This uncertainty range was derived using a set of 100 randomly drawn lens models that provide acceptable fits to account for both the imaging and lensing uncertainties. A fit allowing the ellipticity to vary produces a best fit with  $e = 0.50$ , but a comparison of the residuals for the zero and free ellipticity cases shows no significant improvement when adding these two extra free parameters. Therefore, we assume the zero ellipticity case. For such a compact size we are unable to constrain the Sérsic index of the source, so we fix it to  $n = 1$ . If we use Sérsic indices of 0.5 and 2, the resulting half-light radii lie well within the reported uncertainty. Note that the relatively large uncertainty on  $r_{\text{hl}}$  is a consequence of the uncertainty in the lens model and magnification. As discussed in Section 3.2, the best-fit lens model has relatively low magnification, but the distribution has a tail to higher magnifications. For the size, this results in a tail in the uncertainty distribution towards smaller sizes. The F200W image, best-fit model and residuals are shown in Figure 3.

Using the angular scale at this redshift of 4.74 kpc per arcsec, we determine the physical half-light radius to be  $r_{\text{hl}} = 38_{-19}^{+3}$  pc. This is somewhat smaller than the  $r_{\text{hl}} = 70 \pm 30$  pc determined by Yang et al. (2022) using poorer spatial resolution *HST* imaging. Our size measurement shows CANUCS-A370-z8-LAE to be an extremely compact galaxy.

### 3.4. SED Fitting

The SED-fitting code Bagpipes (Carnall et al. 2018) was used to fit the *JWST* imaging data to derive galaxy physical parameters for CANUCS-A370-z8-LAE. PSF-homogenized photometry in a 0.3" diameter aperture was used to maximize S/N. To avoid issues with correctly fitting the Lyman- $\alpha$  break and emission line region, only wavelengths of 1.5  $\mu\text{m}$  and longer were fit. The redshift is fixed at the spectroscopic redshift. The nebular ionizing parameter was set to  $\log U = -1.5$  motivated by the high observed O32 ratio (Papovich et al. 2022). The models use a Kroupa (2001) Initial Mass

Function. A double power-law star formation history was adopted, but the resulting best fit shows only a steeply rising star formation history, as expected for a galaxy with very high  $\text{EW}(\text{H}\beta)$  and no evidence of a Balmer break in the spectrum or in photometry. Resulting physical parameters from the Bagpipes fit are given in Table 1.

Posterior values of stellar mass and star formation rate were adjusted for an aperture correction from 0.3" to total (Kron) flux of factor 2.3 and for the ‘best’ gravitational lensing magnification of  $\mu = 8.0$  described in Section 3.2. The stellar mass is fairly well constrained for this galaxy (modulo the lensing uncertainty described previously). At this redshift range, the stellar mass can be uncertain for galaxies without spectroscopy because strong emission lines can account for large and uncertain fractions of the F444W flux (e.g. Desprez et al. 2024 find fractions of 0.5 are common). This galaxy has a moderate combined rest-frame equivalent width of [O III] and  $\text{H}\beta$  of 620  $\text{\AA}$  as measured with NIRSPEC, which compares well with the Bagpipes model best fit of 720  $\text{\AA}$ . In addition, the F410M filter is free of strong emission lines, so the rest-frame optical continuum and hence stellar mass is well constrained. The star formation rate from the Bagpipes fit of  $0.54 M_{\odot} \text{ yr}^{-1}$  is quite similar to the star formation rate from the  $\text{H}\beta$  line luminosity of  $0.44 M_{\odot} \text{ yr}^{-1}$ , calculated assuming the relationship of Reddy et al. (2022) for galaxies with low metallicity.

## 4. RESULTS

### 4.1. Metallicity

We determine the gas-phase metallicity of CANUCS-A370-z8-LAE using the strong optical emission lines of  $\text{H}\beta$ , [O III] and the non-detection of [O II]  $\lambda 3727$ . We apply several different calibrations based on local galaxies and distant galaxies observed with *JWST*. The R23 ratio,  $([\text{OIII}](4959+5007)+[\text{OII}]3727)/\text{H}\beta$ , has been found to be the best strong line ratio for low-metallicity galaxies at high-redshift (Laseter et al. 2024; Langeroodi & Hjorth 2024). When combined with O32 ( $[\text{OIII}]5007/[\text{OII}]3727$ ), the two branches of low- and high-metallicity are easily distinguished. This is illustrated in the left panel of Figure 4 where O32 is plotted against R23. The local SDSS galaxies with low R23 have low O32 and consequently have high metallicities and low ionization. In contrast, most  $z > 7$  galaxies observed with *JWST* have high ratios of both R23 and O32, indicating intermediate metallicities ( $\approx 0.1 Z_{\odot}$ ) and high ionization. CANUCS-A370-z8-LAE has the lowest known R23 of  $z > 7$  galaxies, indicating a much lower metallicity. In Figure 4 we highlight the posi-

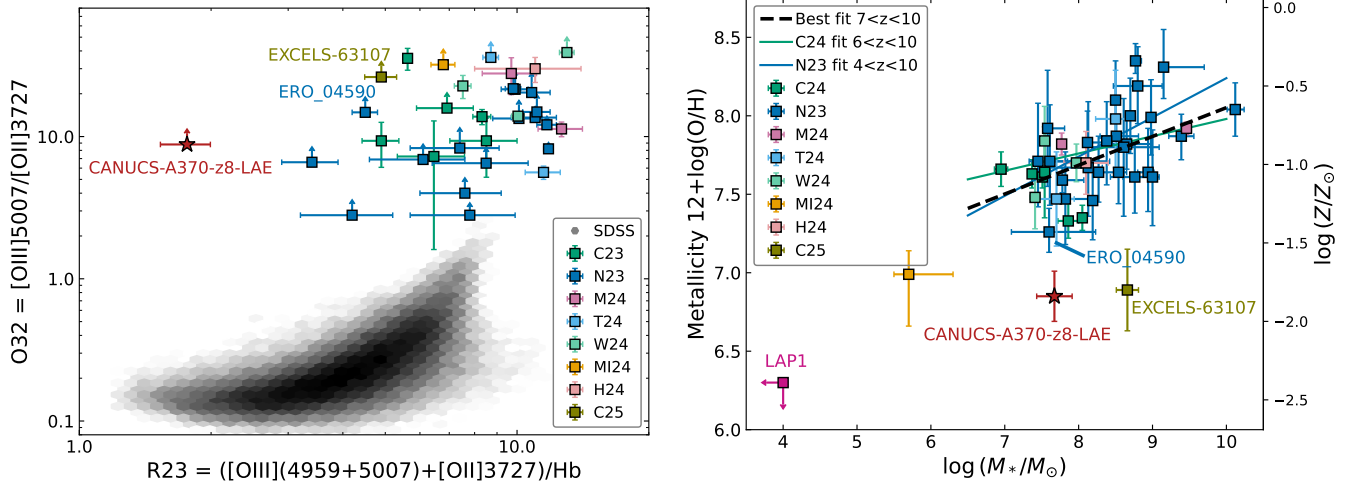


**Figure 4.** Left: Strong emission line ratio diagnostic for redshift  $7 < z < 10$  galaxies with JWST measurements (colored symbols) and SDSS local galaxies (grey density hexmap). CANUCS-A370-z8-LAE has the lowest R23 ratio of known  $z > 7$  galaxies, indicating a very low oxygen abundance. The JWST sample is from JADES (DR1 galaxies from C23: Cameron et al. 2023 and LAEs from W24: Witstok et al. 2025), CEERS, GLASS and SMACS0723-ERO (N23: Nakajima et al. 2023), MACS1149 (M24: Morishita et al. 2024a), Abell1703 (T24: Topping et al. 2024), CANUCS Firefly (MI24: Mowla et al. 2024), MACS0647 JD1 (H24: Hsiao et al. 2024) and EXCELS-63107 (C25: Cullen et al. 2025). Right: Gas-phase metallicity versus stellar mass for a similar sample of  $7 < z < 10$  galaxies. The JADES data, labeled C24, are from Curti et al. 2024 in this plot. Also shown is the very low metallicity lensed star cluster, LAP-1 at  $z = 6.6$  (Vanzella et al. 2023). The mass and metallicity for the Firefly is plotted for a single star cluster (FF-6), since that was the only cluster with measured metallicity (MI24: Mowla et al. 2024). The best fit for the galaxy sample is shown by the black dashed line. This is similar to the best fit relations of Curti et al. (2024) and Nakajima et al. (2023). CANUCS-A370-z8-LAE is a  $4.7\sigma$  outlier relative to the dispersion of other galaxies around the best fit line, with metallicity well below that of other  $7 < z < 10$  galaxies.

tions of two  $z > 8$  galaxies known to have low metallicities from the direct temperature method; ERO\_04590 (Nakajima et al. 2023, see also Curti et al. 2023; Rhoads et al. 2023; Trump et al. 2023) and EXCELS-63107 (Cullen et al. 2025). CANUCS-A370-z8-LAE has a significantly lower R23 ratio than both of these galaxies.

We use R23- $Z_\odot$  relations calibrated from galaxies where direct electron temperatures have been measured from auroral lines. Using the relation of Nakajima et al. (2022) we obtain  $12 + \log(O/H) = 6.88$  or  $0.015 Z_\odot$ . Using the Nakajima et al. (2022) relation for high EW( $H\beta$ ) galaxies would result in a small decrease to  $12 + \log(O/H) = 6.85$  or  $0.014 Z_\odot$ . If instead we use the relation of Curti et al. (2024) we get a similar  $12 + \log(O/H) = 6.81$  or  $0.013 Z_\odot$ . We do not use the Sanders et al. (2024) relation since that relation is not well calibrated at low metallicities, but note that it would lead to substantially lower (0.3 dex) derived metallicity at  $\sim 0.01 Z_\odot$ . We adopt the Nakajima et al. (2022) relation for high EW( $H\beta$ ) galaxies as our nominal metallicity calibration for this galaxy. The uncertainty on the metallicity includes the uncertainty in the empirical calibration.

We do not have a detection of the  $[O III] \lambda 4363$  line to derive the electron temperature and hence use the

direct method of metallicity estimation. However, we note that some other similar extremely compact starbursts at these redshifts show very high electron temperatures and in those cases the direct-method metallicity estimates are considerably lower than their R23-derived values (Nakajima et al. 2023; Mowla et al. 2024; Cullen et al. 2025). This is illustrated by comparing the two panels of Figure 4 for our galaxy, ERO\_04590, Firefly and EXCELS-63107. It is important to obtain deeper spectroscopy at higher resolution to determine if the metallicity of CANUCS-A370-z8-LAE should also be revised even lower.

The mass-metallicity plane is shown in the right panel of Figure 4. CANUCS-A370-z8-LAE is a significant outlier from the distribution defined by  $7 < z < 10$  galaxies from other JWST studies. For context, we also plot on this figure the  $z = 6.6$  lensed star cluster, LAP-1, that has a strong-line metallicity estimate upper limit 0.5 dex lower than that of CANUCS-A370-z8-LAE. We use the plotted sample of  $7 < z < 10$  galaxies from these studies to perform a fit of the mass-metallicity relation. CANUCS-A370-z8-LAE, EXCELS-63107, Firefly and LAP-1 have been published specifically because of their low metallicities, so are excluded from the fit. Using the orthogonal distance regression method of SciPy, we find

a best fit of  $12+\log(\text{O}/\text{H}) = 6.22 + 0.18 \log(M_*/M_\odot)$ . The slope of this relation lies in between those of [Curti et al. \(2024\)](#) and [Nakajima et al. \(2023\)](#). The standard deviation of the galaxy metallicities with respect to the best fit line is 0.16 dex. CANUCS-A370-z8-LAE has a metallicity offset from the best fit line of  $-0.77$  dex and is therefore a  $4.7\sigma$  outlier, with substantially lower metallicity than is typical for galaxies of similar mass at this epoch.

#### 4.2. Lyman- $\alpha$ escape

One of the striking features of the spectrum of CANUCS-A370-z8-LAE is the strong Lyman- $\alpha$  emission line with  $\text{EW}(\text{Ly}\alpha) = 63 \pm 9 \text{ \AA}$  (Figure 1). The detection of this line suggests a considerable fraction of Lyman- $\alpha$  photons are escaping from the galaxy and are transmitted through the CGM (circumgalactic medium) and IGM. We calculate the fraction of escaping photons by considering the ratio between the observed fluxes of Lyman- $\alpha$  and  $\text{H}\beta$ . We do not include any correction for dust, since the nebular dust extinction is not well constrained from the Balmer line ratios (Section 3.1). We find a Lyman- $\alpha$  escape fraction,  $f_{\text{esc}}(\text{Ly}\alpha)$ , of  $0.21 \pm 0.05$  for case B recombination, or  $0.14 \pm 0.04$  for case A. Taking case B as our default value, this is the second-highest known Lyman- $\alpha$  escape fraction at  $z > 8$  after the  $z = 8.28$  galaxy JADES-GN-z8-0-LA ([Tang et al. 2024](#); [Witstok et al. 2025](#); [Jones et al. 2025](#)).

This significant escape fraction of Lyman- $\alpha$  photons requires the galaxy to reside in an ionized bubble. The Lyman- $\alpha$  and continuum fit in Figure 2 is consistent with a Lyman- $\alpha$  line with zero intrinsic offset from the systemic redshift where the galaxy resides in a fully ionized bubble of size 2 pMpc in an otherwise fully neutral IGM. With the limited S/N and resolution of the NIRSpect prism spectrum, we are unable to measure any intrinsic velocity offset or intrinsic line shape, for example if the line is already redshifted and asymmetric as it emerges from the galaxy ISM. An intrinsic redshift of the Lyman- $\alpha$  line of many hundreds of  $\text{km s}^{-1}$  would require a substantially smaller ionized bubble radius for similar Lyman- $\alpha$  transmission ([Dijkstra et al. 2011](#)). However, [Jones et al. \(2025\)](#) show that the typical velocity offset for  $z > 6$  galaxies with such a high escape fraction as ours is only  $200 \text{ km s}^{-1}$ , which would have a very small impact on the derived bubble radius ([Mason & Gronke 2020](#)). It is important to confirm this assumption via future higher resolution spectroscopic observations of Lyman- $\alpha$ .

A symmetric 2 pMpc ionized bubble would be difficult to sustain for a galaxy of this UV luminosity. Fol-

**Table 1.** Properties of CANUCS-A370-z8-LAE

|  |   |
|--|---|
| CANUCS ID                                | 2120090   |
| RA                                       | 39.966109   |
| DEC                                      | $-1.594787$   |
| $z_{\text{spec}}$                        | $8.203 \pm 0.001$   |
| $\mu^\dagger$                            | 8.0   |
| $M_*$                                    | $4.7_{-2.2}^{+2.9} \times 10^7 M_\odot$                           |
| sSFR <sub>BAGPIPES</sub>                 | $1.1 \times 10^{-8} \text{ yr}^{-1}$                              |
| SFR <sub>BAGPIPES</sub>                  | $0.54_{-0.26}^{+0.31} M_\odot \text{ yr}^{-1}$                    |
| SFR <sub>H<math>\beta</math></sub>       | $0.44_{-0.05}^{+0.05} M_\odot \text{ yr}^{-1}$                    |
| $M_{\text{UV}}$                          | $-18.30 \pm 0.12$   |
| UV slope $\beta$                         | $-1.80 \pm 0.15$  |
| $r_{\text{hl}}$                          | $38_{-19}^{+3} \text{ pc}$  |
| EW(Ly $\alpha$ )                         | $63 \pm 9 \text{ \AA}$  |
| EW(H $\beta$ )                           | $225 \pm 50 \text{ \AA}$  |
| EW([O III] $\lambda$ 5007)               | $297 \pm 63 \text{ \AA}$  |
| Flux Ly $\alpha$                         | $77 \pm 10 \times 10^{-19} \text{ erg s}^{-1} \text{ cm}^{-2}$    |
| Flux [O II] $\lambda$ 3727               | $< 2.34 \times 10^{-19} \text{ erg s}^{-1} \text{ cm}^{-2}$       |
| Flux H $\delta$                          | $3.0 \pm 1.3 \times 10^{-19} \text{ erg s}^{-1} \text{ cm}^{-2}$  |
| Flux H $\gamma$                          | $3.9 \pm 1.4 \times 10^{-19} \text{ erg s}^{-1} \text{ cm}^{-2}$  |
| Flux [O III] $\lambda$ 4363              | $1.8 \pm 1.0 \times 10^{-19} \text{ erg s}^{-1} \text{ cm}^{-2}$  |
| Flux H $\beta$                           | $15.6 \pm 1.8 \times 10^{-19} \text{ erg s}^{-1} \text{ cm}^{-2}$ |
| Flux [O III] $\lambda$ 4959              | $6.9 \pm 0.6 \times 10^{-19} \text{ erg s}^{-1} \text{ cm}^{-2}$  |
| Flux [O III] $\lambda$ 5007              | $20.6 \pm 0.6 \times 10^{-19} \text{ erg s}^{-1} \text{ cm}^{-2}$ |
| R23                                      | $1.76 \pm 0.23$   |
| R3                                       | $1.32 \pm 0.15$   |
| O32                                      | $> 8.80$  |
| $12+\log(\text{O}/\text{H})$             | $6.85 \pm 0.16 (0.014 Z_\odot)$                                   |
| $f_{\text{esc}}(\text{Ly}\alpha)$ case B | $0.21 \pm 0.05$   |
| $f_{\text{esc}}(\text{Ly}\alpha)$ case A | $0.15 \pm 0.04$   |
| $\xi_{\text{ion}}$                       | $25.56 \pm 0.08 \text{ Hz erg}^{-1}$                              |

$\dagger$ For a discussion of the uncertainty on the lensing magnification  $\mu$  see Section 3.2. Quoted values of  $M_*$ , SFR and  $M_{\text{UV}}$  are corrected for the best fit  $\mu = 8.0$ , but their uncertainties do not include the additional uncertainty in magnification. The uncertainty on the half-light radius does include the uncertainty in magnification.

lowing the method of [Mason & Gronke \(2020\)](#), we estimate the size of the ionized bubble that the galaxy could generate based on balancing the ionizing photon output rate with recombinations. This method assumes the galaxy is initially embedded in a fully neutral IGM. Assuming the galaxy has been emitting ionizing photons for  $\sim 50 \text{ Myr}$  (c.f. the Bagpipes estimated sSFR of  $\sim 10^{-8} \text{ yr}^{-1}$ ) with a relatively high Lyman continuum escape fraction of 0.5, the expected ionized bubble ra-

dius is  $\approx 0.8$  pMpc. This is substantially lower than the estimated 2 pMpc ionized bubble inferred by the high transmission of Lyman- $\alpha$ .

A possible solution to this inconsistency is that CANUCS-A370-z8-LAE resides in an overdense environment where other galaxies with bursts of star formation at different epochs have combined to produce a larger ionized region. Support for this notion comes from an analysis of spectroscopic redshifts in the field. There are four galaxies with  $z_{\text{spec}} > 8$  in the Abell 370 field measured from CANUCS NIRSpec spectroscopy (Sarrouh and Asada in prep.). Three of these (including CANUCS-A370-z8-LAE) have redshifts equal to within  $\delta z = 0.01$ . The other two galaxies in this redshift interval are CANUCS-2110006 and CANUCS-2111943 with redshifts  $z = 8.199 \pm 0.001$  and  $8.198 \pm 0.004$ , respectively. Of relevance to the environment of CANUCS-A370-z8-LAE, these two other galaxies are located at projected distances of only 0.09 and 0.12 pMpc from CANUCS-A370-z8-LAE, close enough to be contained within the same ionized bubble. We hypothesize that these galaxies, potentially combined with other galaxies in this overdense region, have aided the generation of a relatively large ionized bubble. Further details of these galaxies and the implications for the ionization of the IGM in this region will be presented in Harshan et al. (in prep.).

#### 4.3. Star formation density

With the aid of gravitational lensing, we have strong constraints on the size of CANUCS-A370-z8-LAE, showing it to be extremely compact. From the half-light radius for a symmetric source of  $r_{\text{hl}} = 38_{-19}^{+3}$  pc and taking half of  $\text{SFR}_{\text{H}\beta}$ , we calculate the star-formation rate density,  $\Sigma_{\text{SFR}}$ , within this region to be in the range  $50 - 100 M_{\odot} \text{yr}^{-1} \text{kpc}^{-2}$ , depending on the assumed lensing magnification. This density is significantly higher than local Green Pea galaxies (Yang et al. 2017) and ten times greater than the median for  $7 < z < 9$  galaxies (Morishita et al. 2024b). The SFR density of CANUCS-A370-z8-LAE is comparable to other strong Lyman- $\alpha$ -emitters in the Epoch of Reionization such as COLA-1 (Matthee et al. 2018) and JADES-GN-z8-0-LA (Witstok et al. 2025). The SFR densities of these galaxies are high, considering the Eddington limit for an optically-thick star-forming disk is  $\sim 1000 M_{\odot} \text{yr}^{-1} \text{kpc}^{-2}$  (Thompson et al. 2005). We can speculate that both the high Lyman- $\alpha$  escape fraction and low metallicity may be related to the extreme SFR density (c.f. Pucha et al. 2022).

## 5. DISCUSSION

The discovery of CANUCS-A370-z8-LAE with  $z = 8.203 \pm 0.001$  is important for a few reasons - it is

the first  $z > 7$  galaxy found to have a metallicity approaching 1% solar, its extreme properties, including its compact size ( $r_{\text{hl}} \sim 40$  pc), young age ( $\lesssim 20$  Myr) and high star formation surface density ( $\Sigma_{\text{SFR}} \sim 50 - 100 M_{\odot} \text{yr}^{-1} \text{kpc}^{-2}$ ) indicate a burst of star formation under extreme conditions, and its two close companions suggest that it resides in an ionized bubble at an epoch when the universe was still predominantly neutral. Taken together, these factors provide valuable constraints to test our theories about the mechanisms driving reionization and galaxy evolution at  $z > 8$ .

**Low metallicity:** The exceptionally low metallicity of CANUCS-A370-z8-LAE is particularly noteworthy, as it represents one of the first  $z > 7$  galaxies found with metallicity approaching 1% solar. This finding aligns with theoretical expectations from cosmological simulations like ASTRAEUS that predict the existence of very low metallicity systems at these redshifts, especially in lower-mass halos (Hutter et al. 2021; Legrand et al. 2022). However, the relative scarcity of such low-metallicity objects in current observations (Figure 4) is puzzling. One possible explanation lies in the galaxy's extreme compactness - its  $\approx 40$  pc half-light radius allows us to probe star formation on scales comparable to individual star-forming regions, potentially providing a cleaner window into pristine gas conditions than in more extended systems where metallicity measurements are averaged over larger volumes (James et al. 2020). It is notable that the lowest metallicity object known in the reionization epoch is the strongly-lensed  $z = 6.6$  compact object LAP-1 (Vanzella et al. 2023) that has a mass equivalent to a single star cluster.

**Formation in an overdense region:** The galaxy's environment appears to play a crucial role in its evolution. The presence of two other galaxies within 120 kpc at nearly identical redshifts suggests CANUCS-A370-z8-LAE resides in an overdense region, possibly near a cosmic filament. This environment could explain several of its unique properties. Recent theoretical work (Ocvirk et al. 2021; Harshan et al. 2023) suggests that such overdense regions can experience enhanced cold gas accretion along cosmic filaments, potentially explaining both the intense star formation and low metallicity if this accretion is diluting the existing metal content of the ISM. This scenario is supported by findings from Legrand et al. (2022) showing that galaxies in such environments often experience stochastic star formation histories, particularly at lower masses. Recent observations of low-redshift galaxies demonstrate evidence for episodic star formation fueled by the infall of metal-poor gas (Nakajima et al. 2024). Given the substantial stellar mass built up in this galaxy ( $\sim 5 \times 10^7 M_{\odot}$ ) and

$sSFR \sim 10^{-8} \text{ yr}^{-1}$ , gas dilution is a more likely explanation for the low (1%  $Z_{\odot}$ ) metallicity than the galaxy being in a phase of forming its first generation of stars.

**Ly $\alpha$  emission, UV slope and extreme star formation:** The strong Lyman- $\alpha$  emission ( $EW(\text{Ly}\alpha) = 63 \text{ \AA}$ ) and high escape fraction ( $f_{\text{esc}}(\text{Ly}\alpha) = 0.21$ ) are remarkable given the highly neutral IGM expected at  $z = 8.2$ . Recent work by Witten et al. (2024) demonstrates that tidal interactions and bursty star formation due to merging galaxies can create channels for Lyman- $\alpha$  escape. However, unlike the sample of Ly $\alpha$  emitters of Witten et al. (2024), CANUCS-A370-z8-LAE does not have a merging, close-companion galaxy. The extremely high star-formation rate density suggests that CANUCS-A370-z8-LAE may represent a fundamental mode of early galaxy evolution where star formation proceeds at maximal efficiency. This connects with theoretical work showing that such compact, intense star formation may be crucial for reionization, as the mechanical energy from intense star formation can more efficiently create channels for ionizing photon escape through stellar feedback (Trebitsch et al. 2017; Menon et al. 2024).

The relatively red UV slope ( $\beta = -1.8$ ) presents an interesting puzzle given the low metallicity and strong Lyman- $\alpha$  emission. A similar UV slope is seen in ERO\_04590 ( $\beta = -1.7$ ; Fujimoto et al. 2024) and attributed to moderate dust reddening. These slopes are in stark contrast to EXCELS-63107 that has a very blue UV slope ( $\beta = -3.3$ ; Cullen et al. 2025). While the red slope of CANUCS-A370-z8-LAE could indicate dust enrichment, which seems at odds with the system’s other properties, an alternative explanation may lie in the contribution of nebular continuum emission, consistent with the very high  $H\beta$  equivalent width. However, nebular continuum is expected to have a somewhat bluer slope than seen in CANUCS-A370-z8-LAE, so this aspect remains uncertain. There are also models of massive Population III stars that predict relatively red colors due to re-processing of radiation in inflated stellar envelopes (Woods et al. 2021). Further work is required to model and interpret the complex spectral energy distributions of these galaxies during the Epoch of Reionization.

Taken together, CANUCS-A370-z8-LAE may represent a crucial but short-lived phase in early galaxy evolution where pristine gas accretion, extreme star formation, and efficient feedback processes combine to produce unique observational signatures. Its properties suggest that it may be capturing the moment when one of the Universe’s earliest galaxies is beginning to enrich its surroundings and contribute to cosmic reionization.

## 6. CONCLUSIONS

We have presented JWST imaging and spectroscopy of CANUCS-A370-z8-LAE showing that it is an ultracompact, very low metallicity Lyman- $\alpha$  emitter at  $z = 8.203 \pm 0.001$ . Our key findings are summarized below.

- The R23 ratio of  $1.76 \pm 0.23$  is the lowest of any known  $z > 7$  galaxies, where  $H\beta$  is not enhanced due to the presence of an AGN broad line. The gas-phase metallicity derived from R23 is  $12+\log(\text{O}/\text{H}) = 6.85 \pm 0.16$  or 1.4% solar. The galaxy is a  $4.7\sigma$  outlier from the  $z > 7$  mass-metallicity relation.
- Strong Lyman- $\alpha$  emission is visible in the low-resolution NIRSpect spectrum with  $EW(\text{Ly}\alpha) = 63 \pm 9 \text{ \AA}$ . The Lyman- $\alpha$  escape fraction is estimated to be  $\sim 20\%$ , the second highest known for galaxies at this epoch. The finding of two companion galaxies at the same spectroscopic redshift  $\approx 100 \text{ kpc}$  away suggests an overdensity of galaxies that may have reionized this region and allowed the transmission of Lyman- $\alpha$  photons.
- The galaxy has a half-light radius of only  $\approx 40 \text{ pc}$  and a star formation density  $\Sigma_{SFR} \sim 50 - 100 M_{\odot} \text{ yr}^{-1} \text{ kpc}^{-2}$ . The combination of high SFR density and low metallicity suggests that this galaxy is going through a rare evolutionary stage of rapid cold gas accretion from the cosmic web. The low metallicity is therefore more likely to be due to a recent inflow of low-metallicity gas rather than a young galaxy forming its first stellar populations.

Follow-up spectroscopic observations and observations of similar systems will be crucial for testing our interpretation and refining theoretical models of reionization and galaxy formation in the early Universe.

## ACKNOWLEDGEMENTS

Thanks to Seiji Fujimoto for useful discussions. This research was enabled by grant 18JWST-GTO1 from the Canadian Space Agency and funding from the Natural Sciences and Engineering Research Council of Canada. YA is supported by a Research Fellowship for Young Scientists from the Japan Society of the Promotion of Science (JSPS). MB, JJ, NM, AH and GR acknowledge support from the ERC Grant FIRSTLIGHT and from the Slovenian national research agency ARRS through grants N1-0238 and P1-0188. This research used the Canadian Advanced Network For Astronomy Research (CANFAR) operated in partnership by the Canadian

Astronomy Data Centre and The Digital Research Alliance of Canada with support from the National Research Council of Canada, the Canadian Space Agency, CANARIE and the Canadian Foundation for Innovation.

Data presented in this paper will be made available upon request. The CANUCS DOI is [doi.org/10.17909/ph4n-6n76](https://doi.org/10.17909/ph4n-6n76).

*Facilities:* *JWST* (NIRCam, NIRISS, NIRSpec)

## DATA AVAILABILITY

## REFERENCES

- Annibali, F., & Tosi, M. 2022, *Nature Astronomy*, 6, 48, doi: [10.1038/s41550-021-01575-x](https://doi.org/10.1038/s41550-021-01575-x)
- Arrabal Haro, P., Dickinson, M., Finkelstein, S. L., et al. 2023, *ApJL*, 951, L22, doi: [10.3847/2041-8213/acdd54](https://doi.org/10.3847/2041-8213/acdd54)
- Asada, Y., Desprez, G., Willott, C. J., et al. 2024, arXiv e-prints, arXiv:2410.21543, doi: [10.48550/arXiv.2410.21543](https://doi.org/10.48550/arXiv.2410.21543)
- Birrer, S., & Amara, A. 2018, *Physics of the Dark Universe*, 22, 189, doi: [10.1016/j.dark.2018.11.002](https://doi.org/10.1016/j.dark.2018.11.002)
- Birrer, S., Amara, A., & Refregier, A. 2015, *ApJ*, 813, 102, doi: [10.1088/0004-637X/813/2/102](https://doi.org/10.1088/0004-637X/813/2/102)
- Brammer, G. 2022, *gbrammer/msaexp*: Full working version with 2d drizzling and extraction, 0.3, Zenodo, doi: [10.5281/zenodo.7299501](https://doi.org/10.5281/zenodo.7299501)
- Brammer, G. B., van Dokkum, P. G., & Coppi, P. 2008, *ApJ*, 686, 1503, doi: [10.1086/591786](https://doi.org/10.1086/591786)
- Bromm, V., Coppi, P. S., & Larson, R. B. 1999, *ApJL*, 527, L5, doi: [10.1086/312385](https://doi.org/10.1086/312385)
- Cameron, A. J., Saxena, A., Bunker, A. J., et al. 2023, *A&A*, 677, A115, doi: [10.1051/0004-6361/202346107](https://doi.org/10.1051/0004-6361/202346107)
- Carnall, A. C., McLure, R. J., Dunlop, J. S., & Davé, R. 2018, *MNRAS*, 480, 4379, doi: [10.1093/mnras/sty2169](https://doi.org/10.1093/mnras/sty2169)
- Chen, Z., Stark, D. P., Mason, C., et al. 2024, *MNRAS*, 528, 7052, doi: [10.1093/mnras/stae455](https://doi.org/10.1093/mnras/stae455)
- Cullen, F., Carnall, A. C., Scholte, D., et al. 2025, arXiv e-prints, arXiv:2501.11099, doi: [10.48550/arXiv.2501.11099](https://doi.org/10.48550/arXiv.2501.11099)
- Curti, M., D'Eugenio, F., Carniani, S., et al. 2023, *MNRAS*, 518, 425, doi: [10.1093/mnras/stac2737](https://doi.org/10.1093/mnras/stac2737)
- Curti, M., Maiolino, R., Curtis-Lake, E., et al. 2024, *A&A*, 684, A75, doi: [10.1051/0004-6361/202346698](https://doi.org/10.1051/0004-6361/202346698)
- de Graaff, A., Rix, H.-W., Carniani, S., et al. 2024, *A&A*, 684, A87, doi: [10.1051/0004-6361/202347755](https://doi.org/10.1051/0004-6361/202347755)
- Desprez, G., Martis, N. S., Asada, Y., et al. 2024, *MNRAS*, 530, 2935, doi: [10.1093/mnras/stae1084](https://doi.org/10.1093/mnras/stae1084)
- Dijkstra, M., Mesinger, A., & Wyithe, J. S. B. 2011, *MNRAS*, 414, 2139, doi: [10.1111/j.1365-2966.2011.18530.x](https://doi.org/10.1111/j.1365-2966.2011.18530.x)
- Doyon, R., Willott, C. J., Hutchings, J. B., et al. 2023, *PASP*, 135, 098001, doi: [10.1088/1538-3873/acd41b](https://doi.org/10.1088/1538-3873/acd41b)
- Ferruit, P., Jakobsen, P., Giardino, G., et al. 2022, *A&A*, 661, A81, doi: [10.1051/0004-6361/202142673](https://doi.org/10.1051/0004-6361/202142673)
- Fujimoto, S., Ouchi, M., Nakajima, K., et al. 2024, *ApJ*, 964, 146, doi: [10.3847/1538-4357/ad235c](https://doi.org/10.3847/1538-4357/ad235c)
- Fujimoto, S., Naidu, R. P., Chisholm, J., et al. 2025, arXiv e-prints, arXiv:2501.11678, doi: [10.48550/arXiv.2501.11678](https://doi.org/10.48550/arXiv.2501.11678)
- Gardner, J. P., Mather, J. C., Abbott, R., et al. 2023, *PASP*, 135, 068001, doi: [10.1088/1538-3873/acd1b5](https://doi.org/10.1088/1538-3873/acd1b5)
- Gledhill, R., Strait, V., Desprez, G., et al. 2024, *ApJ*, 973, 77, doi: [10.3847/1538-4357/ad684a](https://doi.org/10.3847/1538-4357/ad684a)
- Harshan, A., Tran, K.-V., Gupta, A., Kacprzak, G. G., & Nanayakkara, T. 2023, *MNRAS*, 522, 1556, doi: [10.1093/mnras/stad959](https://doi.org/10.1093/mnras/stad959)
- Hsiao, T. Y.-Y., Abdurro'uf, Coe, D., et al. 2024, *ApJ*, 973, 8, doi: [10.3847/1538-4357/ad5da8](https://doi.org/10.3847/1538-4357/ad5da8)
- Hutter, A., Dayal, P., Yepes, G., et al. 2021, *MNRAS*, 503, 3698, doi: [10.1093/mnras/stab602](https://doi.org/10.1093/mnras/stab602)
- Ishigaki, M., Kawamata, R., Ouchi, M., et al. 2018, *ApJ*, 854, 73, doi: [10.3847/1538-4357/aaa544](https://doi.org/10.3847/1538-4357/aaa544)
- Izotov, Y. I., Thuan, T. X., Guseva, N. G., et al. 2024, *MNRAS*, 527, 281, doi: [10.1093/mnras/stad3151](https://doi.org/10.1093/mnras/stad3151)
- James, B. L., Kumari, N., Emerick, A., et al. 2020, *MNRAS*, 495, 2564, doi: [10.1093/mnras/staa1280](https://doi.org/10.1093/mnras/staa1280)
- Jones, G. C., Bunker, A. J., Saxena, A., et al. 2025, *MNRAS*, 536, 2355, doi: [10.1093/mnras/stae2670](https://doi.org/10.1093/mnras/stae2670)
- Jung, I., Finkelstein, S. L., Arrabal Haro, P., et al. 2024, *ApJ*, 967, 73, doi: [10.3847/1538-4357/ad3913](https://doi.org/10.3847/1538-4357/ad3913)
- Katz, H., Kimm, T., Ellis, R. S., Devriendt, J., & Slyz, A. 2023, *MNRAS*, 524, 351, doi: [10.1093/mnras/stad1903](https://doi.org/10.1093/mnras/stad1903)
- Kroupa, P. 2001, *MNRAS*, 322, 231, doi: [10.1046/j.1365-8711.2001.04022.x](https://doi.org/10.1046/j.1365-8711.2001.04022.x)
- Langeroodi, D., & Hjorth, J. 2024, arXiv e-prints, arXiv:2409.07455, doi: [10.48550/arXiv.2409.07455](https://doi.org/10.48550/arXiv.2409.07455)
- Laseter, I. H., Maseda, M. V., Curti, M., et al. 2024, *A&A*, 681, A70, doi: [10.1051/0004-6361/202347133](https://doi.org/10.1051/0004-6361/202347133)
- Legrand, L., Hutter, A., Dayal, P., et al. 2022, *MNRAS*, 509, 595, doi: [10.1093/mnras/stab3034](https://doi.org/10.1093/mnras/stab3034)
- Lotz, J. M., Koekemoer, A., Coe, D., et al. 2017, *ApJ*, 837, 97, doi: [10.3847/1538-4357/837/1/97](https://doi.org/10.3847/1538-4357/837/1/97)

- Mason, C. A., & Gronke, M. 2020, *MNRAS*, 499, 1395, doi: [10.1093/mnras/staa2910](https://doi.org/10.1093/mnras/staa2910)
- Matthee, J., Sobral, D., Gronke, M., et al. 2018, *A&A*, 619, A136, doi: [10.1051/0004-6361/201833528](https://doi.org/10.1051/0004-6361/201833528)
- Menon, S. H., Burkhart, B., Somerville, R. S., Thompson, T. A., & Sternberg, A. 2024, arXiv e-prints, arXiv:2408.14591, doi: [10.48550/arXiv.2408.14591](https://doi.org/10.48550/arXiv.2408.14591)
- Morishita, T., Stiavelli, M., Grillo, C., et al. 2024a, *ApJ*, 971, 43, doi: [10.3847/1538-4357/ad5290](https://doi.org/10.3847/1538-4357/ad5290)
- Morishita, T., Stiavelli, M., Chary, R.-R., et al. 2024b, *ApJ*, 963, 9, doi: [10.3847/1538-4357/ad1404](https://doi.org/10.3847/1538-4357/ad1404)
- Mowla, L., Iyer, K., Asada, Y., et al. 2024, *Nature*, 636, 332, doi: [10.1038/s41586-024-08293-0](https://doi.org/10.1038/s41586-024-08293-0)
- Nakajima, K., Ouchi, M., Isobe, Y., et al. 2023, *ApJS*, 269, 33, doi: [10.3847/1538-4365/acd556](https://doi.org/10.3847/1538-4365/acd556)
- Nakajima, K., Ouchi, M., Xu, Y., et al. 2022, *ApJS*, 262, 3, doi: [10.3847/1538-4365/ac7710](https://doi.org/10.3847/1538-4365/ac7710)
- Nakajima, K., Ouchi, M., Isobe, Y., et al. 2024, arXiv e-prints, arXiv:2412.04541, doi: [10.48550/arXiv.2412.04541](https://doi.org/10.48550/arXiv.2412.04541)
- Nishigaki, M., Ouchi, M., Nakajima, K., et al. 2023, *ApJ*, 952, 11, doi: [10.3847/1538-4357/accf14](https://doi.org/10.3847/1538-4357/accf14)
- Ocvirk, P., Lewis, J. S. W., Gillet, N., et al. 2021, *MNRAS*, 507, 6108, doi: [10.1093/mnras/stab2502](https://doi.org/10.1093/mnras/stab2502)
- Oke, J. B., & Gunn, J. E. 1983, *ApJ*, 266, 713, doi: [10.1086/160817](https://doi.org/10.1086/160817)
- Papovich, C., Simons, R. C., Estrada-Carpenter, V., et al. 2022, *ApJ*, 937, 22, doi: [10.3847/1538-4357/ac8058](https://doi.org/10.3847/1538-4357/ac8058)
- Planck Collaboration, Aghanim, N., Akrami, Y., et al. 2020, *A&A*, 641, A6, doi: [10.1051/0004-6361/201833910](https://doi.org/10.1051/0004-6361/201833910)
- Pucha, R., Reddy, N. A., Dey, A., et al. 2022, *AJ*, 164, 159, doi: [10.3847/1538-3881/ac83a9](https://doi.org/10.3847/1538-3881/ac83a9)
- Reddy, N. A., Topping, M. W., Shapley, A. E., et al. 2022, *ApJ*, 926, 31, doi: [10.3847/1538-4357/ac3b4c](https://doi.org/10.3847/1538-4357/ac3b4c)
- Rhoads, J. E., Wold, I. G. B., Harish, S., et al. 2023, *ApJL*, 942, L14, doi: [10.3847/2041-8213/acaaf](https://doi.org/10.3847/2041-8213/acaaf)
- Rieke, M. J., Kelly, D. M., Misselt, K., et al. 2023, *PASP*, 135, 028001, doi: [10.1088/1538-3873/acac53](https://doi.org/10.1088/1538-3873/acac53)
- Rydberg, C.-E., Zackrisson, E., Lundqvist, P., & Scott, P. 2013, *MNRAS*, 429, 3658, doi: [10.1093/mnras/sts653](https://doi.org/10.1093/mnras/sts653)
- Sanders, R. L., Shapley, A. E., Topping, M. W., Reddy, N. A., & Brammer, G. B. 2024, *ApJ*, 962, 24, doi: [10.3847/1538-4357/ad15fc](https://doi.org/10.3847/1538-4357/ad15fc)
- Saxena, A., Robertson, B. E., Bunker, A. J., et al. 2023, *A&A*, 678, A68, doi: [10.1051/0004-6361/202346245](https://doi.org/10.1051/0004-6361/202346245)
- Stark, D. P., Ellis, R. S., Chiu, K., Ouchi, M., & Bunker, A. 2010, *MNRAS*, 408, 1628, doi: [10.1111/j.1365-2966.2010.17227.x](https://doi.org/10.1111/j.1365-2966.2010.17227.x)
- Tang, M., Stark, D. P., Topping, M. W., Mason, C., & Ellis, R. S. 2024, *ApJ*, 975, 208, doi: [10.3847/1538-4357/ad7eb7](https://doi.org/10.3847/1538-4357/ad7eb7)
- Thompson, T. A., Quataert, E., & Murray, N. 2005, *ApJ*, 630, 167, doi: [10.1086/431923](https://doi.org/10.1086/431923)
- Topping, M. W., Stark, D. P., Senchyna, P., et al. 2024, arXiv e-prints, arXiv:2407.19009, doi: [10.48550/arXiv.2407.19009](https://doi.org/10.48550/arXiv.2407.19009)
- Trebitsch, M., Blaizot, J., Rosdahl, J., Devriendt, J., & Slyz, A. 2017, *MNRAS*, 470, 224, doi: [10.1093/mnras/stx1060](https://doi.org/10.1093/mnras/stx1060)
- Tripodi, R., Martis, N., Markov, V., et al. 2024, arXiv e-prints, arXiv:2412.04983, doi: [10.48550/arXiv.2412.04983](https://doi.org/10.48550/arXiv.2412.04983)
- Trump, J. R., Arrabal Haro, P., Simons, R. C., et al. 2023, *ApJ*, 945, 35, doi: [10.3847/1538-4357/acba8a](https://doi.org/10.3847/1538-4357/acba8a)
- Vanzella, E., Loiacono, F., Bergamini, P., et al. 2023, *A&A*, 678, A173, doi: [10.1051/0004-6361/202346981](https://doi.org/10.1051/0004-6361/202346981)
- Venditti, A., Bromm, V., Finkelstein, S. L., Graziani, L., & Schneider, R. 2024, *MNRAS*, 527, 5102, doi: [10.1093/mnras/stad3513](https://doi.org/10.1093/mnras/stad3513)
- Willott, C. J., Doyon, R., Albert, L., et al. 2022, *PASP*, 134, 025002, doi: [10.1088/1538-3873/ac5158](https://doi.org/10.1088/1538-3873/ac5158)
- Willott, C. J., Desprez, G., Asada, Y., et al. 2024, *ApJ*, 966, 74, doi: [10.3847/1538-4357/ad35bc](https://doi.org/10.3847/1538-4357/ad35bc)
- Windhorst, R. A., Timmes, F. X., Wyithe, J. S. B., et al. 2018, *ApJS*, 234, 41, doi: [10.3847/1538-4365/aaa760](https://doi.org/10.3847/1538-4365/aaa760)
- Wise, J. H., Turk, M. J., Norman, M. L., & Abel, T. 2012, *ApJ*, 745, 50, doi: [10.1088/0004-637X/745/1/50](https://doi.org/10.1088/0004-637X/745/1/50)
- Witstok, J., Jakobsen, P., Maiolino, R., et al. 2024, arXiv e-prints, arXiv:2408.16608, doi: [10.48550/arXiv.2408.16608](https://doi.org/10.48550/arXiv.2408.16608)
- Witstok, J., Maiolino, R., Smit, R., et al. 2025, *MNRAS*, 536, 27, doi: [10.1093/mnras/stae2535](https://doi.org/10.1093/mnras/stae2535)
- Witten, C., Laporte, N., Martin-Alvarez, S., et al. 2024, *Nature Astronomy*, 8, 384, doi: [10.1038/s41550-023-02179-3](https://doi.org/10.1038/s41550-023-02179-3)
- Woods, T. E., Willott, C. J., Regan, J. A., et al. 2021, *ApJL*, 920, L22, doi: [10.3847/2041-8213/ac2a45](https://doi.org/10.3847/2041-8213/ac2a45)
- Yang, H., Malhotra, S., Gronke, M., et al. 2017, *ApJ*, 844, 171, doi: [10.3847/1538-4357/aa7d4d](https://doi.org/10.3847/1538-4357/aa7d4d)
- Yang, L., Birrer, S., & Treu, T. 2020, *MNRAS*, 496, 2648, doi: [10.1093/mnras/staa1649](https://doi.org/10.1093/mnras/staa1649)
- Yang, L., Leethochawalit, N., Treu, T., et al. 2022, *MNRAS*, 514, 1148, doi: [10.1093/mnras/stac1236](https://doi.org/10.1093/mnras/stac1236)
- Zackrisson, E., González, J., Eriksson, S., et al. 2015, *MNRAS*, 449, 3057, doi: [10.1093/mnras/stv492](https://doi.org/10.1093/mnras/stv492)